InterPore JOURNAL

Original Research

A HYDRO-GEOMECHANICAL POROUS-MEDIA MODEL TO STUDY EFFECTS OF ENGINEERED CARBONATE PRECIPITATION IN FAULTS

Yue Wang*, Holger Class*

*Institute for Modelling Hydraulic and Environmental Systems, Department of Hydromechanics and Modelling of Hydrosystems, University of Stuttgart, Stuttgart, Germany; *These authors contributed equally to this work.*

Correspondence to:
Yue Wang at
yue.wang@iws.uni-stuttgart.de

How to Cite:
Wang, Y., & Class, H. A (2025). Hydro-Geomechanical Porous-Media Model to Study Effects of Engineered Carbonate Precipitation in Faults. *InterPore Journal*, *2*(2), IPJ040625–6. https://doi.org/10.69631/ipj.v2i2nr41

RECEIVED: 29 Aug. 2024
ACCEPTED: 29 Apr. 2025
PUBLISHED: 4 Jun. 2025

ABSTRACT

Hydro-geomechanical models are required to predict or understand the impact of subsurface engineering applications such as gas storage in geological formations. This study focuses on engineered carbonate precipitation through biomineralization in a fault zone of a cap-rock, aiming to reduce gas leakage from a reservoir. In addition to altering hydraulic properties such as porosity and permeability, precipitated carbonates also change the mechanical properties of the rock. We present a conceptual modeling approach implemented in the open-source simulator DuMu^x. After model verification, we applied the model to a CO_2-storage scenario to investigate how biomineralization affects stress distribution within the rock, as well as how it may alter the risks of fault reactivation and induced seismic events. The generic study shows a tendency towards increased stiffness due to precipitated carbonate, which may cause shear failure events to occur earlier than in an untreated setup, while the magnitude of the seismicity is smaller.

KEYWORDS

Hydro-geomechanical coupling, Biomineralization, Fault reactivation, Model verification

@2025 The Authors

This is an open access article published by InterPore under the terms of the Creative Commons Attribution-NonCommercial-NoDerivatives 4.0 International License (CC BY-NC-ND 4.0) (https://creativecommons.org/licenses/by-nc-nd/4.0/).

1. INTRODUCTION

The injection of large amounts of fluids into the subsurface is a necessary and intentional engineering measure in various technologies that are linked to energy production or storage, such as in geological carbon sequestration, hydraulic fracturing, and geothermal systems. Fluid injections are in some instances also a concomitant feature, for example, when wastewater from conventional or

unconventional hydrocarbon production is re-injected into geological formations. In liberal societies, these technologies are often controversially discussed in view of various risks, which are related to hydro-geomechanical processes and include leakage of fluids or induced seismic events (46).

Leakage from geological reservoirs reduces the efficiency of storage and may pose a threat to the environment. Engineered carbonate precipitation, i.e., the intentional initiation of calcium carbonate formation ($CaCO_3$) through controlled biochemical, chemical, or physical mechanisms, is discussed as a technology that can be implemented in different ways to seal leakage pathways (11, 12, 31, 39, 40). The technology has already progressed successfully from small-scale testing to field-scale application (11). From other ground improvement applications, it is known that induced carbonate precipitation can also enhance the geomechanical properties of porous media (49, 58). However, this aspect so far has been rarely considered in the context of intentional sealing of potential leakage pathways.

Engineered carbonate precipitation can be achieved by various methods, most notably microbially induced carbonate precipitation (MICP), which is distinct from enzymatically induced carbonate precipitation (EICP). While MICP typically relies on the bacterium *Sporosarcina Pasteurii* as a source for the enzyme urease, EICP obtains this enzyme from alternative sources, such as Jack-Bean meal powder. Most importantly, this urease catalyzes the hydrolysis reaction of urea ($(NH_2)_2CO$) into ammonia (NH_3) and carbon dioxide (CO_2). This reaction increases the pH, and aqueous solutions of ammonia become alkaline. More alkalinity in the solution shifts the equilibrium of inorganic carbon species towards higher concentrations of carbonate (CO_3^{2-}). Thus, in the presence of calcium (Ca^{2+}), the precipitation of calcium carbonate ($CaCO_3$) is promoted. The overall reaction is as follows (**Eq. 1**):

$$(NH_2)_2CO+2H_2O+CA^{2+}\rightarrow 2NH_4^{+}+CaCO_3\downarrow \quad (1)$$

The precipitated $CaCO_3$ fills the void in the pore space and alters the mechanical properties of the porous matrix.

While the primary focus of this study was on induced carbonate precipitation (ICP) for targeted sealing of leakage pathways like open fractures, it is worth noting that natural CO_2 mineralization in fractured rock formations has been widely studied and can occur under appropriate conditions. Pilot projects and recent studies, such as those in Nisbet et al (38), indicate that mineralization in fractured rock can be very significant, dependent on the rock type, though the precise role of fractures in promoting this process remains complex. As reviewed in Kim et al (30), factors such as porosity and permeability play crucial roles in CO_2 mineralization. Although changes in mechanical strength have been observed, they have not yet been incorporated into modeling approaches.

Fluid injections into deep subsurface formations influence both fluid pressure and the stress and deformation in geological layers. It is important to understand the hydro-geomechanical couplings to assess and predict potential impacts and risks. One important scenario to consider in such applications is the potential reactivation of existing faults through shear failure. The literature includes several generic studies which reference realistic field-scale applications (3, 6, 33, 45, 48, 50). In some cases, fault reactivation through fluid injections can lead to measurable or even serious seismic events (17, 19, 22, 27, 36, 47).

Numerical simulation of coupled processes is complex and implementations of hydro-geomechanical models are often discussed with respect to numerical accuracy and computational efficiency, since they are typically realized in some kind of appropriate coupling scheme (4, 28, 29, 43, 44). In this study, we present an implementation of a coupled hydro-geomechanical model in the numerical simulator DuMu^{x} [a] (3, 4, 14, 32). The model builds on a recently introduced approach (3, 4) that was originally implemented in an older version of DuMu^{x}. This approach has now been adapted to the current architecture of DuMu^{x} and further developed with respect to the underlying conceptual model. In contrast to the model developed by Loyola et al (34), which extends the non-dimensional fracture model

[a] *DUNE for Multi-{Phase, Component, Scale, Physics, ...} flow and transport in porous media; www.dumux.org*

in DuMu^x and accounts for unevenly developed single-phase flow in fractured areas and uses an upscaling method, our approach maintains an equidimensional description of the fault zone. This allows for the incorporation of mechanical property variations, as the mechanical effects in sub-dimensional regions are ignored. This decision is based on practical considerations for addressing large-scale problems. In the next section, we introduce the basic model concept, including the governing equations and the numerical coupling methods. We extended the approach for the first time to include effects of carbonate precipitation, and we discuss how rock-failure criteria are considered. In addition to the improved conceptual model, we further amended the assembly process by integrating caching techniques into the multi-domain assembler, thereby accelerating its performance and enabling the implementation of the incremental stress formulation.

The model was verified using benchmark problems from related literature, addressing both the coupling flow and geomechanics, as well as the aspects on biomineralization and its implication for geomechanical parameters. In contrast to most hydro-geomechanical simulators, our approach explicitly incorporated effects of precipitation processes in the rock matrix and their mechanical effects. By coupling precipitation-induced changes in porosity and permeability with the material's mechanical response, the model captures alterations in rock stiffness and strength under evolving geochemical conditions. This goes beyond recent (T)HMC models (5, 52), which primarily focus on changes in porosity and rely on empirical relationships to update elastic moduli. In our work, a "cementation" concept was used to mechanistically link precipitation to the rock's stiffness and strength at the pore scale, thus providing a more robust and scalable basis for reservoir-scale and fault-reactivation scenarios. Eventually, the focus of this study was on a reservoir-scale showcase application, where we adapted and extended a fault-reactivation scenario as introduced first by Rutqvist et al (45) and later adopted and modified by others (3, 4). In this study, a showcase scenario was used to investigate how biomineralization of leakage pathways influences the hydrogeomechanical response of a reservoir. Specifically, we wanted to see how sealing acts on the stress state in the reservoir and if continued fluid injection leads to a different pattern of possible failure events. This will be discussed in the context of uncertainties arising from, for example, initial stress distributions, boundary conditions, and inaccuracies in both the model structure and parameter values.

2. MODEL CONCEPTS

2.1. Governing equations

The flow of multiple fluid phases through a deformable porous medium can be mathematically represented by the mass balance equations of the fluids, including Darcy's law as well as the momentum balance of the solid matrix. The equations are coupled via the porosity, i.e., the void space available for fluid, and the pore pressure, i.e., the force exerted on the porous structure by the fluid.

2.1.1. Mass balance equation of the fluid

$$\frac{\partial(\phi_l \varrho_\alpha S_\alpha)}{\partial t} - \mathrm{div}\{\varrho_\alpha \mathbf{v_\alpha}\} - q_\alpha = 0, \alpha \in w, n \tag{2}$$

$\phi_l = (1 + \epsilon_v)\phi$ stands for the absolute void space alteration, while the porosity ϕ represents only the relative ratio in the current reference configuration. ϱ_α, S_α are respectively the density and the saturation of phase α. ϵ_v is the volume strain. Following the assumption of infinitesimal deformation, $\epsilon_v \approx 0$, so $\phi_l \approx \phi$ in this work.

v_α is the Darcy velocity of phase α (**Eq. 3**):

$$v_\alpha = \frac{k_{r\alpha}}{\mu_\alpha}\mathbf{K}(\mathrm{grad}\, p_\alpha - \varrho_\alpha \mathbf{g}) \tag{3}$$

and q_α stands for source or sink terms.

Inserting **Equation 3** into **Equation 2** returns the mass balance equations for the two phase flow (**Eq. 4**):

$$\frac{\partial(\phi\varrho_\alpha S_\alpha)}{\partial t} - \operatorname{div}\left\{\varrho_\alpha \frac{k_{r\alpha}}{\mu_\alpha}\mathbf{K}(\operatorname{grad} p_\alpha - \varrho_\alpha \mathbf{g})\right\} - q_\alpha = 0 \tag{4}$$

The nonlinear storage term in **Equation 4** is equivalent to that in the diffusion equation in Cheng (7) for single phase flow, where the storage term is linearized with **Equation 17** and expressed as **Equation 5**:

$$\frac{\partial(\phi\varrho_)}{\partial t} = \rho\frac{\partial(\alpha\epsilon + \frac{1}{M}p)}{\partial t} \tag{5}$$

with $\alpha[-]$ as Biot coefficient, $\epsilon[-]$ as volume strain of matrix and $M[Pa]$ as Biot Modulus.

The subsequent sections present the verification cases in which the originally employed linear formulations are evaluated against their nonlinear counterparts as implemented within the DuMu^x framework.

2.1.2. Momentum balance of matrix

Adhering to the commonly assumed quasi-static behavior in the field of modelling geomechanics, the momentum balance can be formulated as (**Eq. 6**):

$$\nabla \cdot \boldsymbol{\sigma}_{\text{eff}} + \rho\mathbf{g} = \rho\ddot{\mathbf{u}} \approx 0 \tag{6}$$

where $\varrho = \sum_\alpha \phi S_\alpha \varrho_\alpha + (1-\phi)\varrho_s$ represents the density of the porous medium and $\boldsymbol{\sigma}_{\text{eff}}$ is Biot's effective stress, where positive stress indicates tension (**Eq. 7**):

$$\boldsymbol{\sigma}_{\text{eff}} = \boldsymbol{\sigma} - \alpha p_{\text{eff}}\mathbf{I} \tag{7}$$

with α as Biot's effective stress coefficient, $p_{\text{eff}} = \sum S_\alpha p_\alpha$ as effective pore pressure and $\boldsymbol{\sigma}$ the stress tensor after Hookes Law (**Eq. 8**, **Eq. 9**):

$$\boldsymbol{\sigma} = \lambda\operatorname{tr}(\boldsymbol{\varepsilon})\mathbf{I} + 2G\boldsymbol{\varepsilon} \tag{8}$$

$$\boldsymbol{\varepsilon} = \frac{1}{2}[\nabla\mathbf{u} + (\nabla\mathbf{u})^{\mathrm{T}}] \tag{9}$$

Indeed, the stress tensor σ can also be formulated incrementally. In an incremental approach, the changes in stress are calculated step by step (from $\boldsymbol{\sigma}_{prev}$ to $\boldsymbol{\sigma}$), considering the changes in strain (Δu) and other relevant factors (e.g. variations in bulk modulus) (**Eq. 10**, **Eq. 11**).

$$\boldsymbol{\sigma} = \boldsymbol{\sigma}_{prev} + \lambda\operatorname{tr}(\boldsymbol{\Delta\varepsilon})\mathbf{I} + 2G\boldsymbol{\Delta\varepsilon} \tag{10}$$

$$\boldsymbol{\Delta\varepsilon} = \frac{1}{2}[\nabla(\boldsymbol{\Delta u}) + (\nabla(\boldsymbol{\Delta u}))^{\mathrm{T}}] \tag{11}$$

This method is particularly useful for analyzing materials undergoing alterations, such as the matrix under the reaction of induced carbonate precipitation, and complex loading conditions, where providing a precise description of the displacement is often challenging and not feasible.

Analogous to the incremental stress formulation, the balance equation can also undergo assessment through an incremental approach (**Eq. 12**, **Eq. 13**).

$$\Delta(\nabla \cdot \boldsymbol{\sigma}_{\text{eff}}) + \Delta(\rho\mathbf{g}) = 0 \tag{12}$$

$$\lambda\operatorname{tr}(\boldsymbol{\Delta\varepsilon})\mathbf{I} + 2G\boldsymbol{\Delta\varepsilon} + \Delta(\rho\mathbf{g}) = 0 \tag{13}$$

This method renders the consideration of momentum equilibrium superfluous for the simulation, with the initial stress exclusively influencing the actual in situ stress conditions.

In cases where it is not explicitly mentioned, the incremental stress formulation and incremental momentum local residual are applied by default.

2.1.3. Effective porosity

As aforementioned, the porosity changes are attributable to two factors, the external stress on the solid matrix and the internal pore pressure from a contained fluid.

From the view of micromechanics, as proposed by Gassmann (20) and represented in Cheng (7), and under the assumption of an ideal porous medium (the unjacketed frame bulk modulus $\boldsymbol{K_{s'}}$ and the unjacketed pore volume bulk modulus $\boldsymbol{K_{s''}}$ equal to $\boldsymbol{K_s}$, the bulk module of skeleton formatting solid), the porosity variation as a mechanical response to the altering stress state is defined as **Equation 14**:

$$\Delta\phi = -\frac{\alpha - \phi}{K}\Delta p_T \tag{14}$$

where $\boldsymbol{p_T}$ stands for the Terzaghi effective compressive stress (**Eq. 15**),

$$\Delta p_T = -K\epsilon_v + \Delta[(\alpha - 1)p_{eff}] \tag{15}$$

where ϵ_v is the volume strain of the matrix, and $\boldsymbol{K = \lambda + \frac{2}{3}G}$ is the bulk modulus. The role of pore pressure and Biot coefficient becomes evident when considering the effective compressive stress. In many cases, the Biot coefficient is commonly approximated as $\boldsymbol{\alpha = 1}$, thus the compressive stress primarily depends on the deformation of the matrix.

Substituting **Equation 15** into **Equation 14**, we obtain the effective porosity (**Eq. 16**):

$$\phi = \frac{K\phi_0 - \alpha\Delta p}{K - \Delta p} \tag{16}$$

For a given medium consisting of incompressible solids ($\boldsymbol{\alpha = 1}$), **Equation 16** can be reduced to $\boldsymbol{\phi = \frac{\phi_0 + \mathrm{divU}}{1 + \mathrm{divU}}}$ as in Beck et al (4).

A further linearization of **Equation 14**, based on the characteristic properties of an ideal porous medium, leads to the derivation of **Equation 17**,

$$\Delta\phi = \alpha\epsilon + \frac{1}{M}p_{eff} \tag{17}$$

which is identical to the one in Coussy (8). For details, please refer to the **Appendix A** (**Supplementary Material,** available online).

Equation 14 and **Equation 17** both align with the incremental stress formulation. However, the latter necessitates an explicit calculation of the effective fluid bulk modulus ($\boldsymbol{K_f}$), which becomes considerably intricate in scenarios of two-phase flow involving capillary pressure. Consequently, the first formulation is implemented, wherein $\boldsymbol{K_f}$ is resolved implicitly.

2.1.4. Fixed-stress splitting as decoupling method

By reviewing the mass and momentum balance equations (**Eq. 4**, **Eq. 6**), the coupled system can be solved sequentially: the mass balance equation first predicts the pore pressure under the assumption of a fixed total stress ($\boldsymbol{\Delta\varepsilon_v = 0}$) between two time steps, followed by the momentum equation, which corrects the effective porosity based on the actual pore pressure value. A more detailed algorithm is illustrated in Beck et al (4). However, as pointed out by Mikelić, Wang, and Wheeler (37), the algorithm's efficiency is contingent upon the selection of the "bulk modulus", which, although it can be fictitious and nonphysical, is typically assumed to be equal to the actual bulk modulus of the matrix. Another advantage of this assumption is that it often aligns with boundary conditions commonly used in geomechanics simulations, where a fixed stress—rather than absolute deformation—is taken into consideration.

2.2. Effects of engineered carbonate precipitation on porous media

Precipitated carbonate minerals in a porous medium alter both the hydraulic and mechanical properties of a porous medium. Following the common approach, we used the porosity change to mark the precipitation process. In the following section, we elaborate on how this effect can be qualitatively described.

2.2.1. Mechanical effects

The occupation of void pore volume by precipitation is expected to result in a stiffer and more compact elastic matrix. However, it is worth noting that there are currently only a few available relationships that can describe this phenomenon. Fauriel and Lalouli (18) implemented the linear relationship between shear wave velocity and calcite precipitation, which was observed in the experiment by Qabany et al (42). The two elastic moduli can be determined under the assumption of a constant Poisson's ratio. A similar linear relationship was used in the MICP model proposed by Wang et al (51).

The linear relationship of this kind is straightforward and evident. Nevertheless, its utility remains constrained by the availability of experimental data. Therefore, we suggest a novel approach that incorporates the effect of carbonate precipitation into the natural process, enhancing its adaptability and flexibility.

Cementation of rock is a natural process, by which sediments or grains are bound together by mineral precipitates, creating a solid mass. This crucial geological process plays a significant role in the formation of sedimentary rocks, contributing to their strength and durability over time. Hence, the additional precipitation introduced by the carbonate precipitation process can be conceptually perceived as an enhanced cementation process. Given the assumption that the rock is composed solely of solid grains and cement, and the precipitation has the same chemical structure as the cement so that they cannot be distinguished from one another, we can use the constant cement model concluded in the work of Avseth et al (2) to estimate the mechanical properties of the matrix at each porosity state.

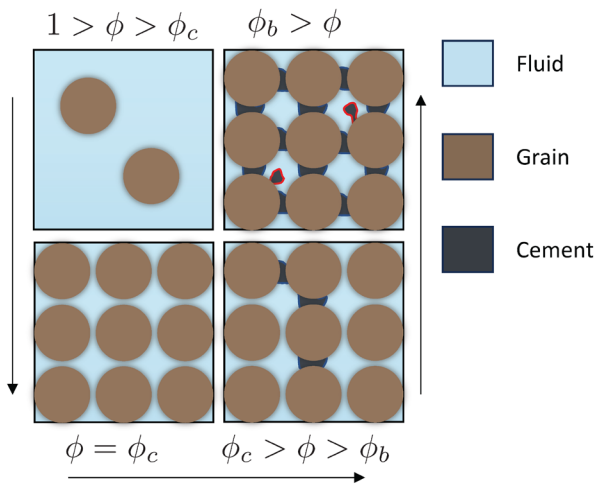


Figure 1: Simplified process (follow subfigures counterclockwise) of rock cementation.

The constant cement model represents a hybrid approach, combining insights from both the contact cement model and the friable-sand model proposed by Dvorkin et al (15, 16). The contact cement model investigates the influence of cement on the contact points between solid grains. This cement layer acts as an elastic foundation during deformation, which can significantly enhance the elastic modulus. On the other hand, the friable-sand model assesses the pressure-dependent bulk modulus of the matrix at the critical porosity, i.e., the porosity at which solid grains start forming a force-bearing structure, and it utilizes the bounding method to refine the modulus range. **Figure 1** illustrates the rock cementation process, depicting the porosity evolution of the matrix. At extremely high porosity, the sand grains remain suspended in the system, with the fluid being the dominant load-bearing element. As sedimentation progresses and sufficient solid grains accumulate, reaching the critical porosity ($\boldsymbol{\phi_c}$), the skeleton of the matrix stabilizes. Subsequently, the cementation process commences, with precipitation initially occurring at the contact points between grains, leading to a significant increase in the matrix's elastic properties. In the final phase, a well-sorted porosity, denoted as $\boldsymbol{\phi_b}$, emerges, signifying that the contact area has been utilized, and precipitation now occurs randomly throughout the matrix. The mathematical description of the constant cement model is provided in **Appendix B** (**Supplementary Material,** available online). This innovative approach has been subjected to comparison with real rock data in Avseth et al (2), as well as exploration through digital rock simulations in Wetzel, Kempka, and Kühn (56).

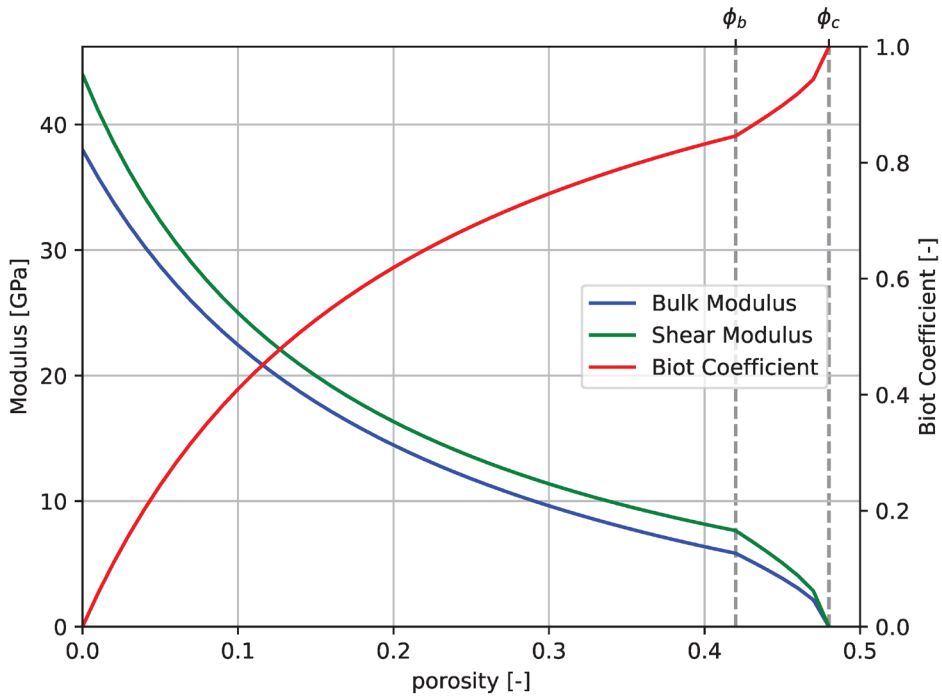


Figure 2: Estimation of rock mechanical properties in response to the cementation.

In contrast to the linear relationship, the constant cement model only relies on material properties and the two porosity parameters ($\boldsymbol{\phi_c}$ and $\boldsymbol{\phi_b}$) that quantify the microstructure of the matrix. The estimated properties with the parameters listed in **Table 1** are plotted in **Figure 2**. By using the relation $\alpha = \mathbf{1} - \frac{\boldsymbol{K}}{\boldsymbol{K_s}}$, the Biot coefficient can be evaluated simultaneously. Nevertheless, it is crucial to note that this is not the proper way to determine this coefficient and caution must be taken, particularly because the Hashin-Shtriktman bound (21) applied in the last phase could lead to significant deviations between the estimated value at low porosity and the actual value.

This description overlooks the dependence on compressional pressure. Therefore, in the simulation, the variation in moduli is only influenced by changes in porosity due to precipitation (in the current case determined by input parameters). The deformation itself does not include this change.

2.2.2. Hydraulic effects

Several experimental studies have provided evidence for the effectiveness of carbonate precipitation in reducing the permeability of porous media; similar insights are reported by studies regarding the mathematical description aimed at quantifying this effect. Hommel et al (23) conducted a comprehensive review of the general formulations concerning the relationship between permeability and porosity with a specific emphasis on induced precipitation. Wetzel et al (55) numerically investigated that changes in permeability can follow distinct rules contingent upon the governing factor, either reaction kinetics or transport processes. From this perspective, the change in permeability is further categorized into two phases, corresponding to the two stages defined in the constant cement model. During the initial phase (referred to as the contact cement model), the permeability exhibits behavior analogous to the Kozeny-Carmen equation (**Eq. 18**) wherein the precipitation primarily impacts the pore throat diameter while preserving the overall shape of the pore throats. In the subsequent phase, a power law model (**Eq. 19**) is applied to account for

Table 1: Parameters for the constant cement model.	
Bulk modulus of grain $\boldsymbol{K_s}$	38 [GPa]
Shear modulus of grain $\boldsymbol{G_s}$	44 [GPa]
Bulk modulus of cement $\boldsymbol{K_c}$	98 [GPa]
Shear modulus of cement $\boldsymbol{G_c}$	35 [GPa]
Critical porosity $\emptyset_c$	0.48 [-]
Well-sorted porosity $\emptyset_b$	0.42 [-]

the distribution of precipitation, which can lead to clogging effects, as previously observed by Weinhardt et al (54).

$$k = \Phi_s^2 \frac{\epsilon^3 D_p^2}{180(1-\epsilon)^2} \tag{18}$$

$$k = b\Phi^n \tag{19}$$

It is worth noting that precipitation can significantly influence the wetting behavior of fluid phases, particularly in the presence of multiple fluid phases (24). In the van Genuchten model, as the reduction in porosity becomes more pronounced, the fitting parameter $\boldsymbol{m}$ tends to increase, while $\boldsymbol{\alpha}$ tends to decrease. Nevertheless, further investigation is necessary to accurately quantify the impact of precipitation on phase behavior in multi-phase systems. In certain unfavorable scenarios, neglecting the heightened capillary pressure at identical saturation levels could potentially lead to unexpected rock shear failure, particularly as the pore pressure approaches critical limits. This aspect will be discussed in the subsequent section. In this paper, for the sake of simplicity, this effect will be approximately represented by adjusting the parameters in the capillary pressure-saturation relationship.

2.3. Rock failure and induced seismic events

In this section, we examine rock failure and fault-zone (re-)activation, along with their associated geomechanical consequences. A commonly employed model in this context is the ubiquitous joint model, using the Mohr-Coulomb criterion with tension cutoff. Since we employed an elastic model, we adopted an approach similar to the previous one, where the adjustment of the stress tensor primarily depends on the failure state, with comparatively less emphasis on ensuring energy conservation. The primary aim of this methodology was to capture and present the phenomenon of rock failure while preserving the focus on the injection-introduced failure behavior.

2.3.1. Residual tensile stress

Rock is commonly recognized as a material with low tensile strength. In our approach, a maximum tensile stress threshold was established, and when the principal stress exceeded this critical value, a cutoff mechanism was triggered. In essence, this cutoff implies the plastic deformation within the rock material.

During the fluid injection process, the vicinity near the injection area is particularly susceptible to tensile failure. Unlike hydraulic fracturing applications, gas injection projects place considerable emphasis on carefully managing the pressure around the injection well to prevent potential tensile failure. Moreover, this study concentrated on investigating the large-scale impacts of the process. Consequently, the consideration of tensile failure was limited to the initial phase, wherein the initial stress was calculated as a result of the geological formation processes.

2.3.2. Shear-stress failure / fault reactivation

Another type of rock failure is the shear-stress failure. When the normal stress acting on the rock matrix is less than the required stress to balance the shear stress, the rock undergoes relative friction, leading to induced seismic events. To analyze this phenomenon, the stress-drop concept proposed in the work

Algorithm 1: Stress tensor adaptation.

$\boldsymbol{\sigma} = \boldsymbol{\sigma}(\boldsymbol{\Delta u}) + \boldsymbol{\sigma}_{\text{prev}}$

// Rotated to principal stress state or by failure angle:

$\boldsymbol{\sigma} = \boldsymbol{R}^T \boldsymbol{\sigma} \boldsymbol{R}$ ▷ $\boldsymbol{R}$ as the rotation tensor

If $\sigma_{xy} > \tau_{\max}$ after Mohr-Coulomb condition **then**

$$\boldsymbol{\sigma} = \begin{bmatrix} \sigma_{xx} & \sigma_{xy} - \Delta\tau \\ \sigma_{yx} - \Delta\tau & \sigma_{yy} \end{bmatrix}$$ ▷ $\Delta\tau$ is stress drop value

end if

Rotated back to original coordination: $\boldsymbol{\sigma} = \boldsymbol{R}\boldsymbol{\sigma}\boldsymbol{R}^{\boldsymbol{\tau}}$

Return $\boldsymbol{\sigma} = \boldsymbol{\sigma} - \boldsymbol{\sigma}_{\text{prev}}$

of Beck et al (3) was employed in this study. This concept postulates that failure occurs at the angle where the shear stress surpasses the allowable threshold. Accordingly, a shear-stress drop occurs at the failure angle, predefined in its magnitude, e.g., 1 MPa. The stress drop is associated with dissipation of the energy, though not modelled. If the rock is situated within the fault zone where the fault angle is known, the stress state at this specific angle is exclusively examined. In such cases, failure occurring within the fault zone is regarded as fault reactivation. **Algorithm 1** demonstrates the modification of the incremental rock stress (relative to the previous state) following this assumption. It is worth noting that even the stress tensor is modified after the stress-drop law, the porosity equation (**Eq. 16**) still holds, since the average pressure $\frac{\boldsymbol{\sigma_{xx}+\sigma_{yy}}}{\mathbf{2}}$ (the center of Mohr Circle) is unchanged.

2.3.3. Estimating seismic events

Both shear-stress failure and fault reactivation have significant implications on the local stress tensor, leading to additional deformation in the rock mass. The evaluation of seismic moments in these scenarios can be accomplished using **Equation 20**:

$$M = G \cdot A \cdot S \tag{20}$$

where $A[\boldsymbol{m^2}]$ represents the area of the crust affected, $\boldsymbol{S}[\boldsymbol{m}]$ corresponds to the average co-seismic deformation, and $\boldsymbol{G}[\boldsymbol{Pa}]$ is the shear modulus at the slip. Again, this moment can be translated to the seismic magnitude with **Equation 21**:

$$M_w = (\log M_0 - 9.1)/1.5 \tag{21}$$

2.4. Simulation workflow of geomechanical problems

The simulation workflow is illustrated in **Algorithm 2**. It can be broadly divided into two steps.

Algorithm 2: Simulation workflow.

Step 1: Initial mechanical conditions

$solve(\boldsymbol{u}_{t_0}\boldsymbol{\sigma}_{t_0})$ ▷ under given hydraulic conditions (e.g. $p_{\alpha,t_0}, s_{\alpha,t_0}$)

Step 2: Time evolution

$solve(\boldsymbol{u}_t, p_{\alpha,t}, s_{\alpha,t})$ with $\Delta\tau = 0$ ▷ no stress drop effect

If $|\tau| > \tau_{max}$ **then** ▷ shear stress failure detected

$solve(u_{t,s}, p_{\alpha,t,s}, s_{\alpha,t,s})$ with $\Delta\tau$

$S = S(\boldsymbol{u}_{t,s} - \boldsymbol{u}_t)$ ▷ calculate slip

$\Delta t = 0.01$ ▷ check for further failures

end if

$t_n \rightarrow t_{n+1}$

In the first step, which may be viewed as a single pre-time step, the initial displacement and stress (**Eq. 4**) is computed based on the boundary conditions and the hydrostatic pressure. In many geomechanics simulations, this step is often skipped, assuming a homogeneous lithostatic pressure. However, it is essential to emphasize that such strong simplifications may not accurately reflect the structural composition of the matrix, potentially underestimating the impact of existing structures.

The second phase, i.e., the main part of the simulation, represents the standard simulation procedure, where we employ the incremental formulation to separate the mechanical effects induced by gas injection. The problem is then solved either in a coupled or decoupled manner, since the hydrostatic pressure is not maintained throughout the simulation. The simulation adheres to a trial pattern, wherein the first step involves calculating the original displacement, excluding the effect of stress drop ($\boldsymbol{\Delta\tau = 0}$). Should any cell undergo shear stress failure, the solution will be adjusted by applying the stress drop value at the failed interface. The total slip S is then quantified as the difference between two states (**Eq. 22**, **Eq. 23**, **Eq. 24**):

$$\boldsymbol{\Delta u} = \mathbf{u}_{t,s} - \mathbf{u}_t \tag{22}$$

$$\mathbf{\Delta} u_{\|} = (\mathbf{\Delta} u \cdot \mathbf{d})\mathbf{d} \tag{23}$$

$$S = \| \mathbf{\Delta u}_{\|,\mathrm{l}} - \mathbf{\Delta u}_{\|,\mathrm{r}} |, \tag{24}$$

where Δu is the differece at nodes and $\Delta_{\|} u$ is the displacement along the fault interface with $\mathbf{d}$ the unit vector of interface.

Upon detecting shear failure, the time step size is sharply reduced to 0.01 s to examine whether the failure propagates to adjacent areas. This implicit method facilitates the determination of relative slip resulting from fault reactivation in fault zone. The induced seismic events are subsequently evaluated using the expression mentioned before as a post-process step.

2.5. Efficient Coding

In DuMu^x, all secondary variables required for the assembly process are encapsulated within the **volumevariables** class. The coupled problem is solved using a multi-domain approach, allowing the utilization of existing models. However, in the current DuMu^x release branch, the caching mechanism for **volumevariables** in the poro-mechanics model is not supported. Given the incremental formulation (**Eq. 11**), a

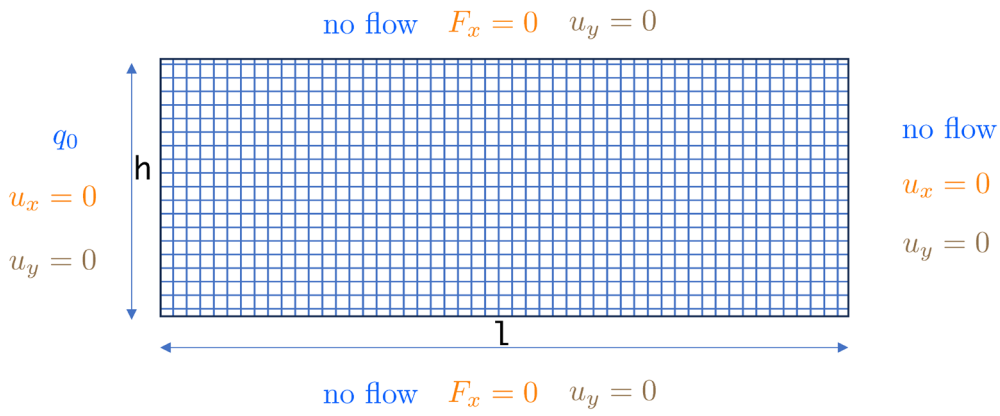


Figure 3: Illustration of domain boundary conditions for the injection problem in the first verification case.

previous state is required for flux assembly, necessitating its availability at all times. To address this, we have updated the caching mechanism to store the stress and secondary variables from the previous time step. This enhancement significantly reduces the computational time required for the assembly process.

3. VERIFICATION

This section aims at demonstrating the successful verification of the introduced model by using various setups and scenarios. The two problems address the standard coupling between flow and geomechanics; they are precisely defined and provide analytical solutions that facilitate verification of the formulations and code implementation.

3.1. Injection Problem

The first problem presented in this study is credited to S. De Simone and J. Carrera and is referred to as Case 3.2 (13). The analytical solution for this problem was developed using the conventional flow equation, with adjustments made to account for hydraulic mechanical responses.

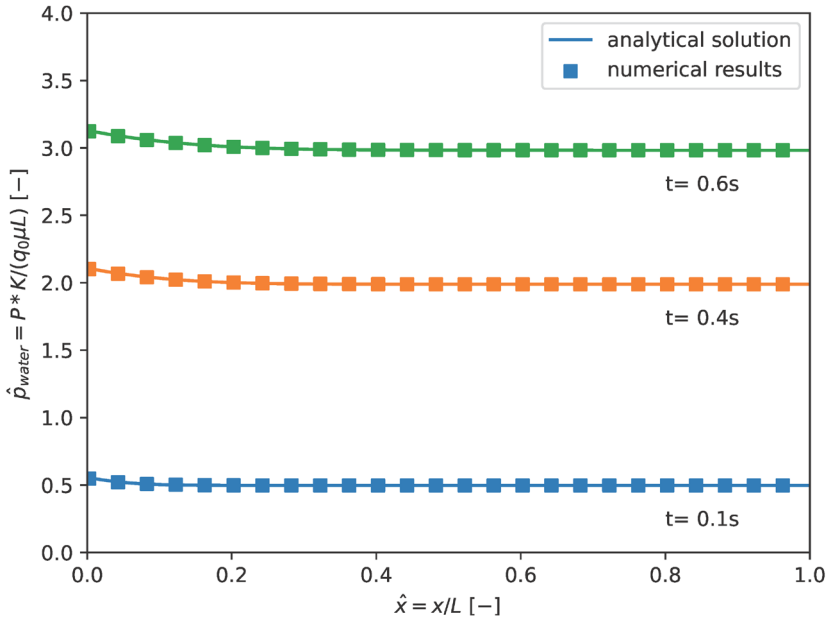


Figure 4: Comparison between the analytical and numerical solutions for the injection problem. $\hat{p}_{Water}$ is equivalent to p_d in Simone and Carrera (13).

The problem domain is defined as a finite region with a length of l and a height of h. Importantly, the geomechanical deformation within this domain is restricted to the x-direction, i.e., the direction of flow. Water is injected from the left boundary, while no-flow boundary conditions are prescribed elsewhere, see **Figure 3**. Due to the symmetry in the y-direction, the complexity of the problem can be reduced, simplifying it into a 1D problem.

De Simone and Carrera (13) employ both local and non-local storage terms to characterize the hydraulic effect and poro-elastic effect (pertaining to the deformation of aquifers), thereby providing an analytical solution to the hydro-mechanical (HM) problem associated with fluid injection in simple geometries. Here, we use the analytical solution as boundary conditions to verify the accurate implementation of equations within the developed DuMu^x model.

Table 2: Parameters for 1D benchmark.

Compressibility of water $\boldsymbol{\beta}$	5e-10 [1/Pa]
Water viscosity $\boldsymbol{\mu}$	1e-3 [Pa·s]
Porosity $\boldsymbol{\phi}$	0.4 [-]
Permeability $\boldsymbol{k}$	1e-10 [m^2]
Biot coefficient $\boldsymbol{\alpha}$	1.0 [-]
Shear modulus $\boldsymbol{G}$	8e6 [Pa]
Lame first constant $\boldsymbol{\lambda}$	12e6 [Pa]

Figure 4 demonstrates the excellent agreement between the analytical and the numerical solutions when employing the incremental formulation along with the previously mentioned porosity alteration relationship (**Eq. 16**), using the input parameters listed in **Table 2**. As the injection process progresses, an over-pressure phenomenon becomes evident throughout the domain. Notably, the over-pressure becomes more significant as we approach the injection boundary.

3.2. Mandel's Problem

Mandel's problem is a well-studied case in poro-elasticity, see (25, 41). It was initially introduced in the paper by Mandel (35), and later extended to anisotropic conditions by Abousleiman et al (1). The problem entails investigating the deformation of a water-saturated 2D matrix subjected to constant-force boundary conditions and the drainage of water. The well-known Mandel-Cryer effect, a hydro-mechanical response, demonstrates the non-monotonic change in water pressure during the drainage process. Due to the intriguing nature of this hydro-mechanics response, Mandel's problem is a valuable choice for evaluating and examining the model.

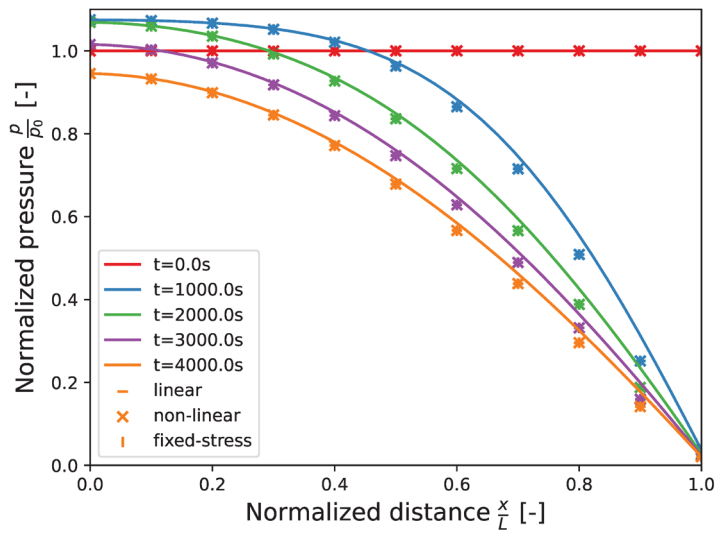


Figure 5: Verification of Mandel's problem.

For verification, only the isotropic case is considered. The analytical solution is simplified from the one in Abousleiman et al (1). Exploring the symmetry of the domain and the boundary condition, only one fourth of the domain is simulated.

Figure 5 demonstrates that our model successfully reproduces the evolution of pressure. In the plot, we compared the results obtained using the linear formulation (**Eq. 5**) with those from our non-linear formulation (**Eq. 4**).

Furthermore, we examined the decoupled scheme (fixed-stress splitting), which yielded converged values identical to those obtained by the fully coupled formulations. Yet, this comparison verifies the accuracy and reliability in incremental formulation by applying the appropriate incremental boundary conditions.

Lastly, we examined the computational improvements attributable to the DuMu^x advancements in cache handling. Under identical conditions, we observed that the assembly time per Newton iteration with caching was reduced from 0.25 seconds to 0.125 seconds, corresponding to an approximate 50% reduction. Notably, the solution time for the linear solver remained unchanged.

4. COMPARISON BETWEEN SIMULATED AND EXPERIMENTAL DATA OF AN EICP-TREATED SAND COLUMN

The constant cement model was originally proposed to analyze rock formation and the mechanical role of cement (2). We propose utilizing this model in our study to predict the evolving mechanical properties of the matrix at varying porosity or cement content. Apparently, there is a need to test its applicability and to get a better understanding of its limitations.

Due to the lack of well-documented and well-controlled experimental data on real core samples undergoing biomineralization, we have employed the experimental data for artificially produced sand columns from the study conducted by Yasuhara et al (57). In their study, the authors created columns using EICP methods, wherein they initially mixed Toyoura Sand with the urease (enzyme) before injecting cementation solutions ($CaCl_2$ and urea) from the bottom into the sand column (5 cm in diameter and 10 cm in height) under fully saturated and compressed conditions. Following several injections, the cementation process bonded the sand particles together to form samples for further testing. Subsequently, the column was dried out, and an acid leaching method was employed to measure the weight and volume occupied by the cement. Additionally, the authors conducted unconfined compression strength (UCS) tests on the samples for mechanical properties. A group of experiments were conducted, varying in the mixing ratio of sand and urease, the concentration of the cement solution, and number of injections. The initial sand samples had a porosity of $\phi_{ini} = 0.44$ and the acid leaching revealed that calcite cement accounted for approximately 0.01 to 0.04 of the column's volume. The UCS tests showed a range of the secant elastic modulus at 50% of the peak strength E_{50} values from 53.5 to 160 MPa. Additionally, the results of X-ray diffractometry (XRD) confirmed that quartz (grain material) and calcite (cement material) are the main components of the treated sand columns.

The conducted experiment aligns with the requirements of the constant cement model, as the parameters needed for this model can be directly deduced from the experimental data, including the UCS and porosity data by Yasuhara et al (57) as the reference for the predictions provided by the constant cement model. Given that our focus in this section is on the mechanical aspect, we exclusively simulate the UCS tests of dry samples as a purely mechanical process. The setup and balance equations are listed in **Appendix C** in the **Supplementary Material** (available online). We use a 2D domain (2.5 cm in radius and 10 cm in height) to represent the half of the column cross section, under the strong assumption that the distribution of precipitation within the column samples is axially symmetric. The compressive force is represented as the displacement of rigid surface on the top, while the average normal stress on the top is considered as the value obtained from the UCS test. The load velocity of strain is set at $0.045\% \frac{cm}{cm \cdot s}$, with the simulation ending at a total strain of 0.45%. Elastic moduli of quartz ($K_s = 38\ GPa, G_s = 44\ GPa$) and calcite ($K_c = 63\ GPa, G_c = 31\ GPa$), critical porosity $\phi_c = \phi_{ini} = 0.44$ are given as input parameters to the constant cement model. However, there is no direct data available for estimating the important value of the well-sorted porosity ϕ_b, and thus, we adopt a range from 0.40 to 0.44, as suggested in other work (9). Furthermore, we consider the heterogeneity of precipitation distribution, as the chemical processes may be influenced by flow conditions within the column. Due to limited data on local porosity, we assume a linear porosity profile (0.39 at the bottom and 0.43 at the top) to investigate the role that the porosity profile plays.

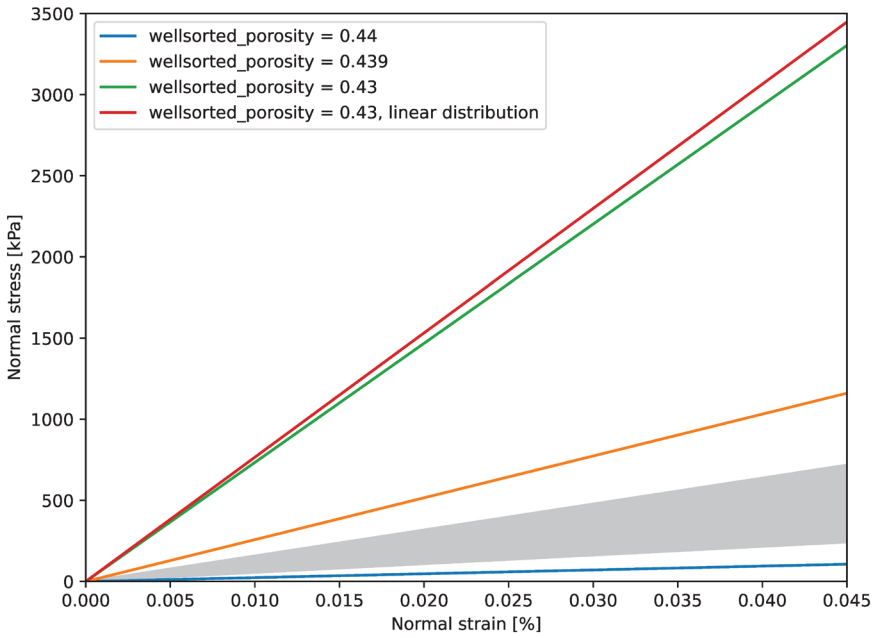


Figure 6: Fictive Unconfined Compression Test Protocol. The gray area represents the measurement in experiments of (57).

Figure 6 depicts a hypothetical protocol of UCS tests. The experiments show a range of E_{50} values from 53.5 to 160 MPa, while the simulated values range from 23 to 734 MPa. The results indicate that the constant cement model is highly sensitive to the well-sorted porosity. Experimental measurements indicate the well-sorted porosity to fall within a narrow range from 0.439 to 0.44, suggesting potential difference in sorting between natural sands of greater non-uniformity and those used in the Yasuhara et al experiments (57). Nonetheless, this finding supports the notion that some precipitation occurs at the contact area, enhancing the compressibility of the entire column. Lastly, the results indicate further that an uneven distribution, in conjunction with the non-linearity in the cement model, could lead to a higher effective E_{50} strength.

In summary, the constant cement model demonstrates applicability in predicting strength of EICP-treated porous media, while the range of predictions for these reference experiments is large. We should note that the model is quite simple, requiring only a few details; on the other hand, knowledge of the required data is also limited. We suppose that a particular difficulty in transferring insights from these reference data to realistic rocks is the uniformity of grain sizes and heterogeneities, which are likely higher in realistic cases, and, therefore, the sensitivity of the predicted strength to the well-sorted porosity is smaller. In any case, the observed discrepancies highlight the need for further research on detecting and analyzing the role of local precipitation and parameterization.

5. EFFECTS OF BIOMINERALIZATION ON GEOMECHANICS IN A RESERVOIR INJECTION SCENARIO

Building upon the validated and tested model as detailed in the preceding sections, we have developed a simulation scenario to examine the practical implications of cementation processes in underground gas storage systems. The scenario is inspired by the CO_2 storage framework proposed by Mazzoldi et al (36), which investigates the potential for fault reactivation and induced seismicity during underground CO_2 injection. In this study, we extended the framework to include the effects of biomineralization, with a continued emphasis on fault reactivation, while explicitly excluding rock failure within the matrix. Given the significant uncertainty associated with strength predictions, as highlighted in the previous section, this scenario is intended as a case study to discuss the implications of biomineralization, utilizing results that are believed to represent reasonable orders of magnitude.

5.1. Scenario definition

As shown in **Figure 7**, the proposed two-dimensional domain measures 2 km by 2 km, with a depth range from 500 m to 2500 m. The storage layer, which is 100 meters thick, is bound above and below by less permeable rock layers, each 150 meters thick. These bounding layers are themselves surrounded by

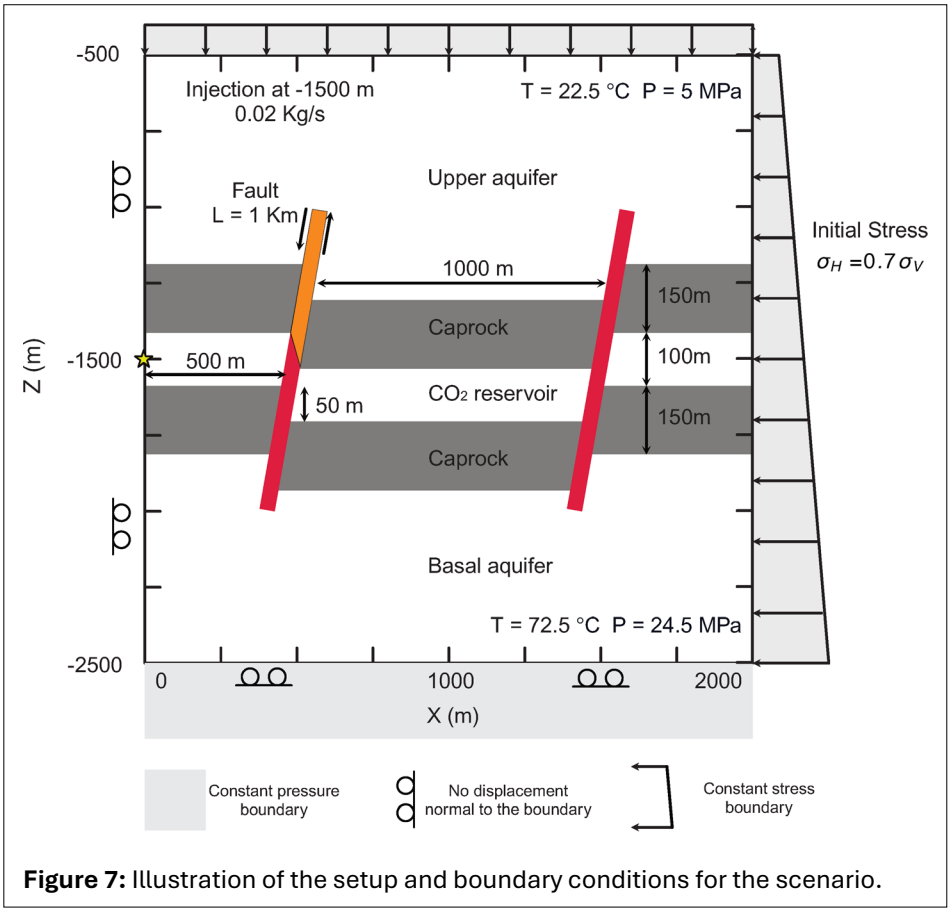


Figure 7: Illustration of the setup and boundary conditions for the scenario.

two other formations that have a permeability comparable to the storage layer. To investigate the latent effects of biomineralization on the original geological condition, we modified the fault zone configuration by introducing a second fault zone and adjusting the offset of two faults. Within the subsurface, two fault zones are present at a distance of 1 km apart, each with a dip angle of 80° and a width of 10 meters, intersecting the storage layer. In this showcase scenario, we assume that the more permeable left fault zone is detectable and indicates the need for biomineralization, whereas the less permeable right fault zone remains untreated.

In practical terms, biomineralization will only seal the upper section of the left fault zone, as indicated by the orange marking in **Figure 7**. These fault zones initially exhibit a shear displacement offset (throw) of 50 meters, resulting in a hydraulically confined reservoir. Specifically, the left fault zone has a positive throw of 50 meters, while the right fault zone exhibits a negative throw of 50 meters. Carbon dioxide is injected from the left boundary at a constant rate of $0.0004\ \mathrm{kg/(m^2 \cdot s)}$, corresponding to $630.72\ \mathrm{t/year/m}$ for a site extending 100 m in length. The injection process is terminated upon detecting fault reactivation in any of the fault zones, with the simulation concluding in all cases after 100 days.

Three distinct test cases are defined to evaluate the effects of different treatment strategies on fault zones. Case A serves as the baseline scenario, in which neither of the fault zones receives any treatment, allowing for natural conditions to be observed. In Case B, a targeted partial zone undergoes slight sealing through induced biomineralization, representing a moderate intervention. Case C involves an intensive treatment of the fault zone, which significantly reduces porosity. This scenario examines the impact of extensive biomineralization on the structural properties of the fault zone.

Table 3: Summary of material properties by Geological Zone.

		Caprock	Reservoir	Upper Aquifer	Basel Aquifer	Right Fault	Left Fault		
							A	B	C
	Porosity [-]	0.01	0.1	0.1	0.01	0.1	0.15	0.07	0.05
Hydraulic	Van Genuchten α [1/Pa]	5.025×10^{-5}	5.025×10^{-4}	5.025×10^{-4}	5.025×10^{-4}	5.025×10^{-4}	5.025×10^{-4}	1.675×10^{-4}	1.675×10^{-4}
Hydraulic	Van Genuchten N [-]	1.842	1.842	1.842	1.842	1.842	1.842	0.368	0.368
Hydraulic	Permeability [m^2]	1×10^{-19}	1×10^{-13}	1×10^{-14}	1.9×10^{-16}	1×10^{-15}	1.9×10^{-13}	1.9×10^{-14}	7×10^{-15}
Mechanical	Biot Coefficient [-]	0.242	0.778	0.778	0.778	-	-	-	-
Mechanical	Bulk Modulus [MPa]	34.4	6.0	6.0	6.0	-	-	-	-
Mechanical	Shear Modulus [MPa]	18.7	8.0	8.0	8.0	-	-	-	-
Mechanical	Critical Porosity [-]	-	-	-	-	0.105	0.155	0.155	0.155
Mechanical	Well Sorted Porosity [-]	-	-	-	-	0.07	0.12	0.12	0.12

The hydraulic and mechanical parameters are presented in detail in **Table 3**. For the left fault zone, the parameters are divided into three cases, with the lower part of the zone remaining unchanged across all simulations, using the same values as those listed for Case A. The initial porosities correspond to the general values used in the original setup. For moderate and intensive treatments, reductions of 8% and 10% in porosity, respectively, are considered. Based on experimental observations in Weinhardt et al (54), the permeability of the treated fault zones is calculated using the power law described in **Equation 19**, with $n = 3$, resulting in a reduction by an order of magnitude. The parameters for the Van Genuchten Model are estimated based on experimental trends observed by (24), with general factors of 0.33 and 0.2 applied for V_α and V_n, respectively in both cases, as the actual porosity approaches.

The mechanical part employs the constant cement model, utilizing the parameters outlined in **Table 1**. The bulk and shear moduli are directly assigned for specific geological zones, rather than being treated

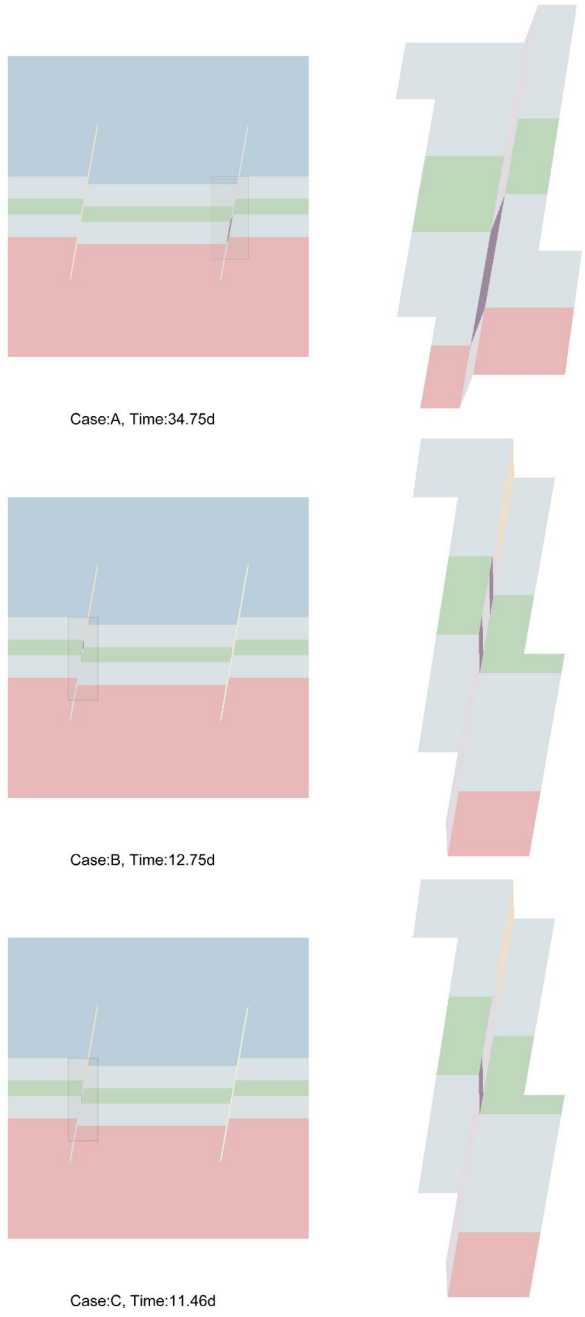


Figure 8: Visualization of cells experiencing shear stress failure during the initial failure event. The colors represent the different zone types, with the darkest color indicating the failed zones. The time indicated in the figure corresponds to the moment when the first failure event occurs.

as fitted parameters, to ensure consistency with other simulations. For the fault zones, the critical porosities are assumed to be slightly higher than the initial porosity, reflecting the potential for poorly cemented structures within the geological formations. Furthermore, the well-sorted porosity is set to be 3.5% less than the critical value.

5.2. Results

In three instances, a single injection-induced shear failure event was observed at 34.75 days, 12.75 days, and 11.46 days, respectively. These observations indicate that a less permeable and more robustly sealed zone leads to faster failure events. In addition to influencing the timing of occurrence, the biomineralization process also alters the failure position. **Figure 8** illustrates the locations of the failed cells in each scenario. In the absence of biomineralization, failure occurred at the intersection of the less permeable right fault zone and the lower rock layer. When bio-mineralization is applied, primary failures shift to the left fault zone. All failures occurred then in the untreated left fault zone and remained within the reservoir layer. In Case B, two failure cells were detected at the connection points to the neighboring rock layer, whereas in the stronger cemented Case C, only the lower cell experienced shear stress failure. Here, we focus on the ICP effect within the fault zone; additional results concerning injection-related pressure and stress changes are provided in **Appendix D** (**Supplementary Material**, available online).

We use the concept of "pressure safety margin" to indicate the maximum allowed pressure change necessary to prevent triggering shear stress failure (**Eq. 25**):

$$\tau' = (\sigma' - \alpha P_{Pore} - P_{Safety})\tan\phi + c \tag{25}$$

where τ' and σ' represent the shear stress and normal stress along the fault direction, respectively.The parameters ϕ and c denote the friction angle and cohesion coefficient, as defined in the Coulomb–Mohr theory. This margin can also be interpreted as the distance from the failure curve line to the Mohr circle.

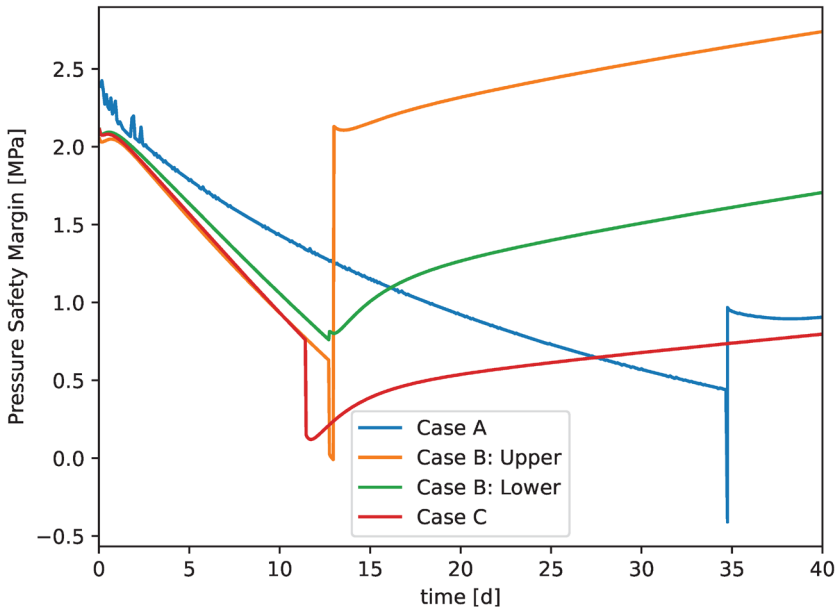


Figure 9: Time-dependent safety margin of failed cells across different cases.

Notably, as the safety margin approaches zero, the system becomes highly sensitive to shear failure. **Figure 9** shows the change in the pressure safety margin of selected cells over time. In Case A, we selected the cell with the most significant stress change as the representative one. The two cells in Case B and the single cell in Case C are also plotted. The timing of the dramatic drop in the safety margin corresponds to occurrences of shear stress failure, although the drop value (ranging from 0.1 MPa to 2.2 MPa) does not match the shear stress drop value (1.0 MPa). All curves confirm that the induced stress drop enhances safety subsequently after the shear stress drop. It is also apparent that the safety margin value drops at a similar rate in the treated cases (B and C) during the injection period.

A further analysis of the stress tensor indicates that the principal stress state is very close to the physical configuration, with an angle of less than 2 degrees. The local rotated stress state along the fault zone is also similar to the principal one, as the dip angle of the fault zone is nearly parallel to the axis. **Figure 10** provides more details about the temporal evolution of the stress and pressure states in the failed cells.

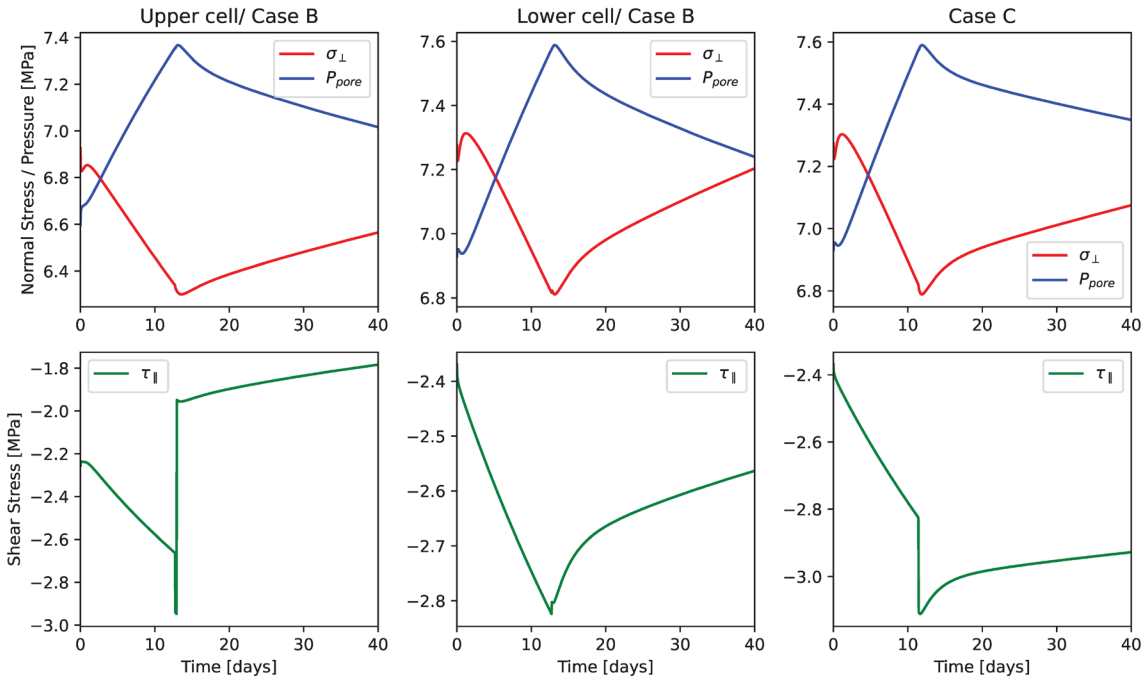


Figure 10: Time evolution of normal compressive stress and shear stress on the fault plane, as well as the effective pore pressure change for the failed cells in Cases B and C.

 https://doi.org/10.69631/ipj.v2i2nr41

σ_τ represents the normal compressive stress (positive for compression) on the fault plane, while τ denotes the local shear stress on the fault zone. The injection operation results in an increase in pore pressure (around 1 MPa) and shear stress (around 0.4 MPa), as well as a decrease in normal compressive stress (around 0.5 MPa). Additionally, the shear stress change in the lower cell in Case B shows a significant difference in stress drop value, while the other cell exhibits only a slight change.

The difference in displacement and slip of the fault zone in each case is depicted in **Figure 11**. In Case A, significant deformation occurs within 0.03 s, where shear failure in the initially failed cell also triggers the adjacent cells, resulting in substantial slip at the end. The displacement in the other two cases is of a similar magnitude, where we observe opposite slip directions and pronounced asymmetrical displacement. Assuming a field length of 100 m, the slips correspond to seismic events of magnitudes 1.16, 0.63, and 0.64. It is evident that mineralization alters the positions where seismic events are triggered but effectively reduces seismic energy since the occurrence is earlier. However, it is important to note that an earlier occurrence of failure does not necessarily indicate a lower intensity.

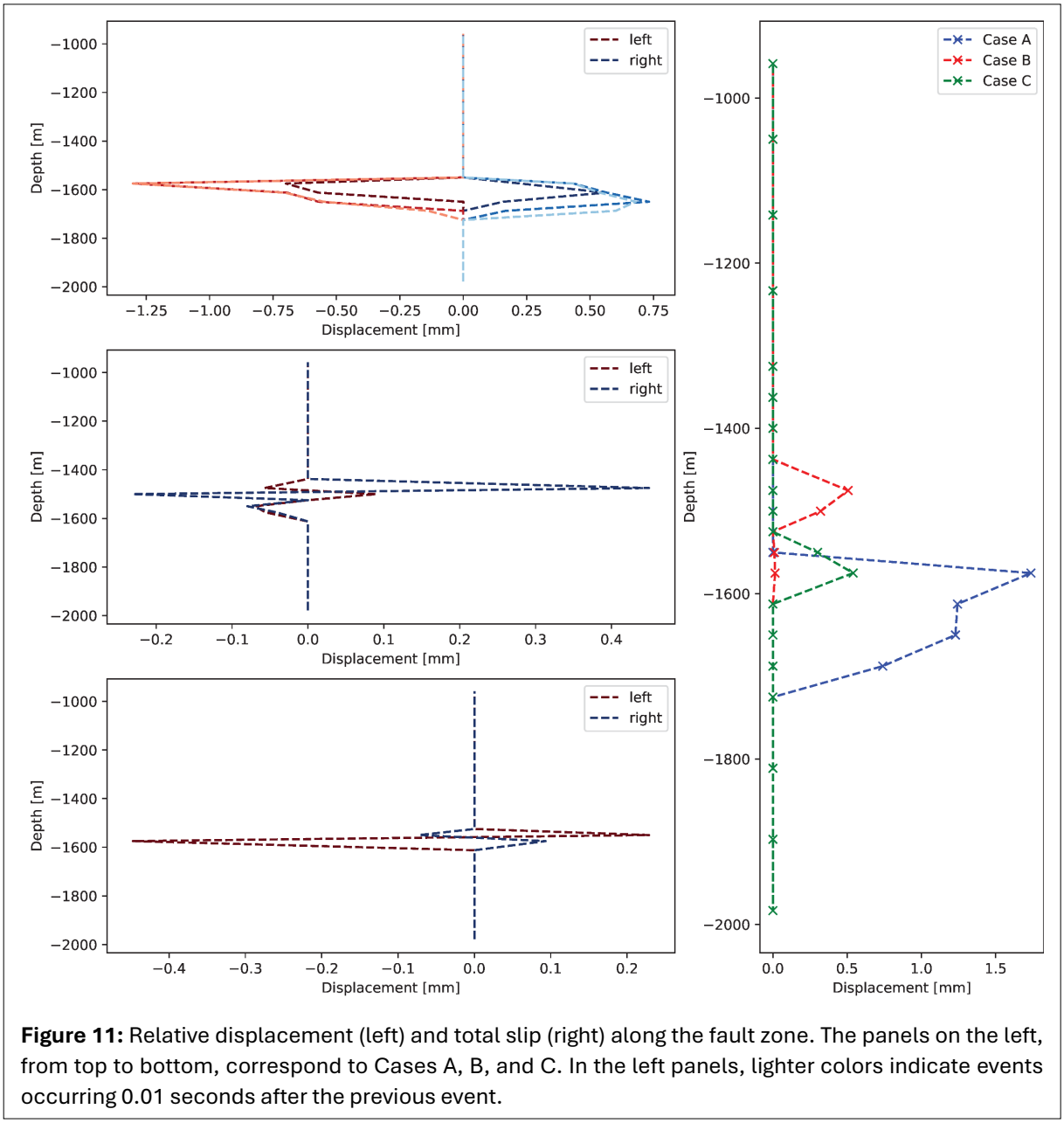


Figure 11: Relative displacement (left) and total slip (right) along the fault zone. The panels on the left, from top to bottom, correspond to Cases A, B, and C. In the left panels, lighter colors indicate events occurring 0.01 seconds after the previous event.

 https://doi.org/10.69631/ipj.v2i2nr41

6. DISCUSSION AND CONCLUSIONS

Sealing flow paths to prevent leakage is a primary target of biomineralization and affects the hydraulic properties, in particular porosity and permeability. Beyond that, the results of the showcased scenarios highlight the practical potential impact of biomineralization on geomechanical properties and events in underground gas storage. Gas injection reduces compressive stress due to the effective stress effect and simultaneously induces additional shear stress within the domain to maintain elastic deformation of the subsurface. This result is significant, as it aligns with reported events observed in real-world field operations. However, this effect is subject to variations in geological formations and boundary conditions, which are not covered in the showcase.

Within the proposed scenarios, a locally sealed fault zone slightly affects the flow paths for injected gas. However, the rapid buildup of pressure, due to fluid compression and the pressure gradient required for flow, depletes the pressure safety margin. This depletion may explain why the failure is shifted. In addition to the hydraulic effects, the process also increases the stiffness of the fault zone. A higher elastic modulus allows for smaller deformations, resulting in less additional shear stress, which enhances the safety of the matrix. However, it also decreases the homogeneity of the domain, causing weaker sections to undergo larger deformations and potentially fail, as observed in this case.

A different extent of the biomineralization process exhibits similar changes in effective pore pressure and shear stress. This similarity can be attributed to the flow field not being strongly affected. However, the displacement of the cells shows a markedly different pattern of deformation, which can be attributed to the occurrence of failure at different positions. In Case B, the upper failed cell undergoes most of the slip, providing the lower cell with additional freedom. In contrast, in Case C, the failed cell is located in the lower half of the domain and lacks adjacent cells to absorb the additional energy, resulting in deformation in a different direction. As shown in **Figure 2**, the variation in properties demonstrates that a stiffer sealed fault zone results in increased plastic deformation in the surrounding weaker regions. This observation is further corroborated by the corresponding seismic energy levels.

Focusing on the energy levels, it is apparent that biomineralization results in much smaller seismic activities compared to the cases without biomineralization. In contrast to the aftershocks reported in Keranen et al (26), no post-injection seismic events were detected. This can be attributed to the setup and characteristics of the proposed system, where failures occur much earlier and injections stop immediately after the occurrence. However, given the rather low intensity of the activity, an instantaneous response is unfeasible in practical scenarios, leading to a substantial buildup of pore pressure. This lack of buildup also contributes to the absence of post-injection events in the modelled scenarios.

The presented study demonstrates the potential effects of biomineralization in a gas-storage scenario with fault zones. However, the results are highly dependent on the specific geometric setup and model parameters, making them site-specific and difficult to generalize. While the model could be applied to CO_2 mineralization scenarios, this was beyond the scope of the study. The constant cement model used relies on several parameters that should be validated with real-world data, and the study did not account for local effects or heterogeneity within the geological zone. From an engineering perspective, many operational possibilities remain unexplored. Despite the promising results, several limitations should be noted. The constant cement model is heuristic and simplifies the mechanical properties of rock grains, cements, and porosity parameters, which can vary widely in reality. The permeability-porosity relationships depend on experimental data, but do not fully account for the spatial distribution of mineral precipitation, indicating the need for more detailed subscale analyses. Moreover, the model assumes small deformations and linear elasticity, limiting its applicability to more complex or non-linear geological scenarios. Future work should refine these assumptions, integrate more comprehensive experimental data, and extend the framework to include more sophisticated mechanical and flow behavior to improve model robustness and applicability.

In conclusion, we can summarize this study as follows:

- We further developed and updated the geomechanical model of the open-source simulation platform DuMu^x to its latest version. This update preserves the stress drop concept from previous work to describe shear stress failure, while employing an incremental formulation as an interface to facilitate future improvements and enhance computational efficiency. The model was tested and successfully verified against benchmarks from the literature.
- We developed and applied a method to integrate changes in the hydraulic and mechanical properties of porous media under biomineralization. These effects are linked to pore space alteration, and a preliminary comparison with models and experimental data from the literature demonstrates the potential of this approach.
- We further applied the proposed model to investigate the potential effects of biomineralization on the field scale of underground gas storage scenarios. Although the showcased scenario relies on a significant abstraction of reality, our study demonstrates that this process can alter system behavior and reduce damage to the fault zone. Additionally, the simulations highlight the intricate effects of coupled processes (sealing effect vs. seismic energy) inherent to the showcased scenario, which must be accounted for in real-world decision-making procedures. A well-sealed fracture is essential for preventing leakage, whereas a significant reduction in permeability—along with a corresponding increase in stiffness—can influence potential seismic events. A deeper understanding of these relations is needed to inform engineering practice.

STATEMENTS AND DECLARATIONS

Supplementary Material

All appendices to this material are available online and can be downloaded here.

Acknowledgements

We thank the Deutsche Forschungsgemeinschaft (DFG, German Research Foundation) for supporting this work by funding SFB 1313, Project Number 327154368

Author Contributions

Both authors contributed equally to the design and implementation of the research, to the analysis of the results and to the writing of the manuscript.

Conflicts of Interest

There are no conflicts of interest to declare.

Data, Code & Protocol Availability

The code is available as a dataset hosted at the data repository of the University of Stuttgart (DaRUS)(53) and as a DuMu^x -pub module https://git.iws.uni-stuttgart. de/dumux-pub/wang2024a, accessed on 29 August 2024.

ORCID IDs

Yue Wang https://orcid.org/0000-0002-9455-7621
Holger Class https://orcid.org/0000-0002-4476-8017

REFERENCES

1. Abousleiman, Y., Cheng, A. H.-D., Cui, L., Detournay, E., & Roegiers, J.-C. (1996). Mandel's problem revisited. *Géotechnique*, 46(2), 187–195. https://doi.org/10.1680/geot.1996.46.2.187
2. Avseth, P., Mukerji, T., Mavko, G., & Dvorkin, J. (2010). Rock-physics diagnostics of depositional texture, diagenetic alterations, and reservoir heterogeneity in high-porosity siliciclastic sediments and rocks—A review

of selected models and suggested work flows. *GEOPHYSICS*, 75(5), 75A31-75A47. https://doi.org/10.1190/1.3483770
3. Beck, M., & Class, H. (2019). Modelling fault reactivation with characteristic stress-drop terms. *Advances in Geosciences*, 49, 1–7. https://doi.org/10.5194/adgeo-49-1-2019
4. Beck, M., Rinaldi, A. P., Flemisch, B., & Class, H. (2020). Accuracy of fully coupled and sequential approaches for modeling hydro- and geomechanical processes. *Computational Geosciences*, 24(4), 1707–1723. https://doi.org/10.1007/s10596-020-09987-w
5. Bhukya, P. K., Adla, N., & Arnepalli, D. N. (2024). Coupled bio-chemo-hydro-mechanical modeling of microbially induced calcite precipitation process considering biomass encapsulation using a micro-scale relationship. *Journal of Rock Mechanics and Geotechnical Engineering*, 16(7), 2775–2789. https://doi.org/10.1016/j.jrmge.2023.09.023
6. Cappa, F., & Rutqvist, J. (2011). Modeling of coupled deformation and permeability evolution during fault reactivation induced by deep underground injection of CO_2. *International Journal of Greenhouse Gas Control*, 5(2), 336–346. https://doi.org/10.1016/j.ijggc.2010.08.005
7. Cheng, A. H.-D. (2016). *Poroelasticity* (Vol. 27). Springer International Publishing. https://doi.org/10.1007/978-3-319-25202-5
8. Coussy, O. (2003). *Poromechanics* (1st ed.). Wiley. https://doi.org/10.1002/0470092718
9. Critical-porosity models. (2001). In A. R. Huffman & G. L. Bowers, *Pressure Regimes in Sedimentary Basins and Their Prediction* (pp. 33–41). American Association of Petroleum Geologists. https://doi.org/10.1306/M76870C4
10. Cunningham, A. B., Class, H., Ebigbo, A., Gerlach, R., Phillips, A. J., & Hommel, J. (2019). Field-scale modeling of microbially induced calcite precipitation. *Computational Geosciences*, 23(2), 399–414. https://doi.org/10.1007/s10596-018-9797-6
11. Cunningham, A. B., Phillips, A. J., Troyer, E., Lauchnor, E., Hiebert, R., Gerlach, R., & Spangler, L. (2014). Wellbore leakage mitigation using engineered biomineralization. *Energy Procedia*, *63*, 4612–4619. https://doi.org/10.1016/j.egypro.2014.11.494
12. Cuthbert, M. O., McMillan, L. A., Handley-Sidhu, S., Riley, Michael. S., Tobler, D. J., & Phoenix, Vernon. R. (2013). A field and modeling study of fractured rock permeability reduction using microbially induced calcite precipitation. *Environmental Science & Technology*, 47(23), 13637–13643. https://doi.org/10.1021/es402601g
13. De Simone, S., & Carrera, J. (2017). Analytical solutions to coupled hm problems to highlight the nonlocal nature of aquifer storage. *Water Resources Research*, 53(11), 9580–9599. https://doi.org/10.1002/2017WR020824
14. *DuMux Handbook*. (n.d.). DuMux Organisation. https://dumux.org/docs/
15. Dvorkin, J., Mavko, G., & Nur, A. (1991). The effect of cementation on the elastic properties of granular material. *Mechanics of Materials*, 12(3–4), 207–217. https://doi.org/10.1016/0167-6636(91)90018-U
16. Dvorkin, J., Nur, A., & Yin, H. (1994). Effective properties of cemented granular materials. *Mechanics of Materials*, 18(4), 351–366. https://doi.org/10.1016/0167-6636(94)90044-2
17. Ellsworth, W. L. (2013). Injection-induced earthquakes. *Science*, 341(6142), 1225942. https://doi.org/10.1126/science.1225942
18. Fauriel, S., & Laloui, L. (2012). A bio-chemo-hydro-mechanical model for microbially induced calcite precipitation in soils. *Computers and Geotechnics*, 46, 104–120. https://doi.org/10.1016/j.compgeo.2012.05.017
19. Frohlich, C., Ellsworth, W., Brown, W. A., Brunt, M., Luetgert, J., MacDonald, T., & Walter, S. (2014). The 17 May 2012 *M* 4.8 earthquake near Timpson, East Texas: An event possibly triggered by fluid injection. *Journal of Geophysical Research: Solid Earth*, 119(1), 581–593. https://doi.org/10.1002/2013JB010755
20. Gassmann, F. (1951). *Über die elastizität poröser medien*. Inst. für Geophysik an der ETH.
21. Hashin, Z., & Shtrikman, S. (1963). A variational approach to the theory of the elastic behaviour of multiphase materials. *Journal of the Mechanics and Physics of Solids*, 11(2), 127–140. https://doi.org/10.1016/0022-5096(63)90060-7
22. Holland, A. A. (2013). Earthquakes triggered by hydraulic fracturing in south-central oklahoma. *Bulletin of the Seismological Society of America*, 103(3), 1784–1792. https://doi.org/10.1785/0120120109
23. Hommel, J., Coltman, E., & Class, H. (2018). Porosity–permeability relations for evolving pore space: A review with a focus on (Bio-)geochemically altered porous media. *Transport in Porous Media*, 124(2), 589–629. https://doi.org/10.1007/s11242-018-1086-2
24. Hommel, J., Gehring, L., Weinhardt, F., Ruf, M., & Steeb, H. (2022). Effects of enzymatically induced carbonate precipitation on capillary pressure–saturation relations. *Minerals*, 12(10), 1186. https://doi.org/10.3390/min12101186

25. Keilegavlen, E., Berge, R., Fumagalli, A., Starnoni, M., Stefansson, I., Varela, J., & Berre, I. (2021). PorePy: An open-source software for simulation of multiphysics processes in fractured porous media. *Computational Geosciences*, 25(1), 243–265. https://doi.org/10.1007/s10596-020-10002-5
26. Keranen, K. M., Savage, H. M., Abers, G. A., & Cochran, E. S. (2013). Potentially induced earthquakes in Oklahoma, USA: Links between wastewater injection and the 2011 Mw 5.7 earthquake sequence. *Geology*, 41(6), 699–702. https://doi.org/10.1130/G34045.1
27. Keranen, K. M., Weingarten, M., Abers, G. A., Bekins, B. A., & Ge, S. (2014). Sharp increase in central Oklahoma seismicity since 2008 induced by massive wastewater injection. *Science*, 345(6195), 448–451. https://doi.org/10.1126/science.1255802
28. Kim, J. (n.d.). *Sequential methods for coupled geomechanics and multiphase flow | suetri-b reservoir simulation*. Retrieved May 26, 2025, from https://suetri-b.stanford.edu/publications/theses/sequential-methods-coupled-geomechanics-and-multiphase-flow
29. Kim, J., Moridis, G. J. J., Yang, D., & Rutqvist, J. (2012). Numerical studies on two-way coupled fluid flow and geomechanics in hydrate deposits. *SPE Journal*, 17(02), 485–501. https://doi.org/10.2118/141304-PA
30. Kim, K., Kim, D., Na, Y., Song, Y., & Wang, J. (2023). A review of carbon mineralization mechanism during geological CO_2 storage. *Heliyon*, 9(12), e23135. https://doi.org/10.1016/j.heliyon.2023.e23135
31. Kirkland, C. M., Thane, A., Hiebert, R., Hyatt, R., Kirksey, J., Cunningham, A. B., Gerlach, R., Spangler, L., & Phillips, A. J. (2020). Addressing wellbore integrity and thief zone permeability using microbially-induced calcium carbonate precipitation (Micp): A field demonstration. *Journal of Petroleum Science and Engineering*, 190, 107060. https://doi.org/10.1016/j.petrol.2020.107060
32. Koch, T., Gläser, D., Weishaupt, K., Ackermann, S., Beck, M., et al. (2021). DuMux 3 – an open-source simulator for solving flow and transport problems in porous media with a focus on model coupling. *Computers & Mathematics with Applications*, *81*, 423–443. https://doi.org/10.1016/j.camwa.2020.02.012
33. Lei, X., Huang, D., Su, J., Jiang, G., Wang, X., et al. (2017). Fault reactivation and earthquakes with magnitudes of up to Mw4.7 induced by shale-gas hydraulic fracturing in Sichuan Basin, China. *Scientific Reports*, 7(1), 7971. https://doi.org/10.1038/s41598-017-08557-y
34. Loyola, A. C., Cordão Neto, M. P., & Pereira, J.-M. (2024). An open-source numerical laboratory to assess the poromechanical behavior of fractured rocks. *Computers and Geotechnics*, 168, 106127. https://doi.org/10.1016/j.compgeo.2024.106127
35. Mandel, J. (1953). Consolidation des sols(Étude mathématique). *Géotechnique*, 3(7), 287–299. https://doi.org/10.1680/geot.1953.3.7.287
36. Mazzoldi, A., Rinaldi, A. P., Borgia, A., & Rutqvist, J. (2012). Induced seismicity within geological carbon sequestration projects: Maximum earthquake magnitude and leakage potential from undetected faults. *International Journal of Greenhouse Gas Control*, 10, 434–442. https://doi.org/10.1016/j.ijggc.2012.07.012
37. Mikelić, A., Wang, B., & Wheeler, M. F. (2014). Numerical convergence study of iterative coupling for coupled flow and geomechanics. *Computational Geosciences*, 18(3–4), 325–341. https://doi.org/10.1007/s10596-013-9393-8
38. Nisbet, H., Buscarnera, G., Carey, J. W., Chen, M. A., Detournay, E., et al. (2024). Carbon mineralization in fractured mafic and ultramafic rocks: A review. *Reviews of Geophysics*, *62*(4), e2023RG000815. https://doi.org/10.1029/2023RG000815
39. Phillips, A. J., Cunningham, A. B., Gerlach, R., Hiebert, R., Hwang, C., et al. (2016). Fracture sealing with microbially-induced calcium carbonate precipitation: A field study. *Environmental Science & Technology*, 50(7), 4111–4117. https://doi.org/10.1021/acs.est.5b05559
40. Phillips, A. J., Troyer, E., Hiebert, R., Kirkland, C., Gerlach, R., et al. (2018). Enhancing wellbore cement integrity with microbially induced calcite precipitation (Micp): A field scale demonstration. *Journal of Petroleum Science and Engineering*, 171, 1141–1148. https://doi.org/10.1016/j.petrol.2018.08.012
41. Phillips, P. J., & Wheeler, M. F. (2007). A coupling of mixed and continuous Galerkin finite element methods for poroelasticity I: The continuous in time case. *Computational Geosciences*, 11(2), 131. https://doi.org/10.1007/s10596-007-9045-y
42. Qabany, A. A., Mortensen, B., Martinez, B., Soga, K., & DeJong, J. (2011). Microbial carbonate precipitation: Correlation of s-wave velocity with calcite precipitation. *Geo-Frontiers* 2011, 3993–4001. https://doi.org/10.1061/41165(397)408
43. Rinaldi, A. P., Rutqvist, J., & Cappa, F. (2014). Geomechanical effects on CO_2 leakage through fault zones during large-scale underground injection. *International Journal of Greenhouse Gas Control*, 20, 117–131. https://doi.org/10.1016/j.ijggc.2013.11.001
44. Rutqvist, J., Birkholzer, J. T., & Tsang, C.-F. (2008). Coupled reservoir–geomechanical analysis of the potential for tensile and shear failure associated with CO_2 injection in multilayered reservoir–caprock systems.

International Journal of Rock Mechanics and Mining Sciences, 45(2), 132–143. https://doi.org/10.1016/j.ijrmms.2007.04.006
45. Rutqvist, J., Rinaldi, A. P., Cappa, F., & Moridis, G. J. (2013). Modeling of fault reactivation and induced seismicity during hydraulic fracturing of shale-gas reservoirs. *Journal of Petroleum Science and Engineering*, 107, 31–44. https://doi.org/10.1016/j.petrol.2013.04.023
46. Scheer, D., Class, H., & Flemisch, B. (2021). *Subsurface environmental modelling between science and policy*. Springer International Publishing. https://doi.org/10.1007/978-3-030-51178-4
47. Shapiro, S. A., & Dinske, C. (2009). Fluid-induced seismicity: Pressure diffusion and hydraulic fracturing. *Geophysical Prospecting*, 57(2), 301–310. https://doi.org/10.1111/j.1365-2478.2008.00770.x
48. Sibson, R. H. (1985). A note on fault reactivation. *Journal of Structural Geology*, 7(6), 751–754. https://doi.org/10.1016/0191-8141(85)90150-6
49. Van Paassen, L. A., Ghose, R., Van Der Linden, T. J. M., Van Der Star, W. R. L., & Van Loosdrecht, M. C. M. (2010). Quantifying biomediated ground improvement by ureolysis: Large-scale biogrout experiment. *Journal of Geotechnical and Geoenvironmental Engineering*, 136(12), 1721–1728. https://doi.org/10.1061/(ASCE)GT.1943-5606.0000382
50. Vilarrasa, V., & Carrera, J. (2015). Geologic carbon storage is unlikely to trigger large earthquakes and reactivate faults through which CO_2 could leak. *Proceedings of the National Academy of Sciences*, 112(19), 5938–5943. https://doi.org/10.1073/pnas.1413284112
51. Wang, X., Bhukya, P. K., Arnepalli, D. N., & Chen, S. (2024). Coupled multiphysical model for investigation of influence factors in the application of microbially induced calcite precipitation. *Journal of Rock Mechanics and Geotechnical Engineering*, 16(6), 2232–2249. https://doi.org/10.1016/j.jrmge.2024.03.007
52. Wang, X., & Nackenhorst, U. (2022). Micro-feature-motivated numerical analysis of the coupled bio-chemo-hydro-mechanical behaviour in MICP. *Acta Geotechnica*, 17(10), 4537–4553. https://doi.org/10.1007/s11440-022-01544-2
53. Wang, Y., & Class, H. (2025). *A hydro-geomechanical porous-media model to study effects of engineered carbonate precipitation in faults* (arXiv:2504.05171). arXiv. https://doi.org/10.48550/arXiv.2504.05171
54. Weinhardt, F., Deng, J., Hommel, J., Vahid Dastjerdi, S., Gerlach, R., Steeb, H., & Class, H. (2022). Spatiotemporal distribution of precipitates and mineral phase transition during biomineralization affect porosity–permeability relationships: Microfluidic investigations. *Transport in Porous Media*, 143(2), 527–549. https://doi.org/10.1007/s11242-022-01782-8
55. Wetzel, M., Kempka, T., & Kühn, M. (2020). Hydraulic and mechanical impacts of pore space alterations within a sandstone quantified by a flow velocity-dependent precipitation approach. *Materials*, 13(14), 3100. https://doi.org/10.3390/ma13143100
56. Wetzel, M., Kempka, T., & Kühn, M. (2021). Diagenetic trends of synthetic reservoir sandstone properties assessed by digital rock physics. *Minerals*, 11(2), 151. https://doi.org/10.3390/min11020151
57. Yasuhara, H., Neupane, D., Hayashi, K., & Okamura, M. (2012). Experiments and predictions of physical properties of sand cemented by enzymatically-induced carbonate precipitation. *Soils and Foundations*, 52(3), 539–549. https://doi.org/10.1016/j.sandf.2012.05.011
58. Zeng, C., Veenis, Y., Hall, C. A., Young, E. S., Van Der Star, W. R. L., et al. (2021). Experimental and numerical analysis of a field trial application of microbially induced calcite precipitation for ground stabilization. *Journal of Geotechnical and Geoenvironmental Engineering*, 147(7), 05021003. https://doi.org/10.1061/(ASCE)GT.1943-5606.0002545